

# A chemically etched D-band waveguide orthomode transducer for CMB measurements

E. Manzan<sup>1,2</sup>, A. Mennella<sup>1,2\*</sup>, F. Cavalieri<sup>1,2</sup>, C. Franceschet<sup>1,2</sup>, S. Mandelli<sup>1,2</sup>, F. Montonati<sup>1</sup>, M. Zannoni<sup>3,4</sup>, P. de Bernardis<sup>5,6</sup>, M. Bersanelli<sup>1,2</sup>, E. Boria<sup>1</sup>, N. Brancadori<sup>1</sup>, A. Coppolecchia<sup>5,6</sup>, M. Gervasi<sup>3,4</sup>, L. Lamagna<sup>5,6</sup>, A. Limonta<sup>3,4</sup>, S. Masi<sup>5,6</sup>, A. Paiella<sup>5,6</sup>, A. Passerini<sup>3,4</sup>, F. Pezzotta<sup>1,2</sup>, G. Pettinari<sup>7</sup>, F. Piacentini<sup>5,6</sup>, E. Tommasi<sup>8</sup>, D. Vigano<sup>2</sup>, A. Volpe<sup>8</sup>

<sup>1</sup>Università degli studi di Milano, Milano, Italy.

<sup>2</sup>INFN sezione di Milano, Milano, Italy.

<sup>3</sup>Università di Milano Bicocca, Milano, Italy.

<sup>4</sup>INFN sezione di Milano Bicocca, Milano, Italy.

<sup>5</sup>Università di Roma La Sapienza, Roma, Italy.

<sup>6</sup>INFN sezione di Roma 1, Roma, Italy.

<sup>7</sup>CNR/IFN - Consiglio Nazionale delle Ricerche, Roma, Italy.

<sup>8</sup>ASI - Agenzia Spaziale Italiana, Roma, Italy.

\*Corresponding author(s). E-mail(s): [aniello.mennella@fisica.unimi.it](mailto:aniello.mennella@fisica.unimi.it);

## Abstract

This study presents a prototype D-band waveguide orthomode transducer (OMT) fabricated using chemically etched brass platelets. This method offers a fast, cost-effective, and scalable approach for producing waveguide OMTs above 100 GHz, making it well-suited for current and future Cosmic Microwave Background polarization experiments, where large focal planes with thousands of receivers are required to detect the faint primordial *B*-modes. Chemical etching has already demonstrated its effectiveness in manufacturing corrugated feedhorn arrays with state-of-the-art performance up to 150 GHz. Here, we evaluate its applicability to more complex structures, such as OMTs.

We designed a single OMT prototype operating in the 130–170 GHz range, fabricated by chemically etching 0.15 mm-thick brass plates, which were then stacked, aligned, and mechanically clamped. Simulations based on metrological measurements of the OMT profile predict return losses below  $-10$  dB, isolation better than  $-30$  dB, and transmission around  $-0.5$  dB.

The measured transmission and isolation, however, is around  $-1.5$ – $-2$  dB and  $< -20$  dB, respectively. Further simulations show that the degradation in the transmission is related to defects and roughness along the etched profile ( $\text{RMS} \simeq 3 \mu\text{m}$ ), which is a typical and unavoidable effect of chemical etching. The discrepancy in isolation, instead, could arise from a slight rotation ( $\sim 3^\circ$ ) of the polarization angle within the measurement chain.

Our results show that chemical etching is a fast, low-cost, and scalable technique for producing waveguide OMTs with state-of-the-art performance in terms of return loss and isolation. However, at frequencies above 100 GHz the transmission coefficient may degrade due to the mechanical precision limitations of chemical etching.

**Keywords:** Orthomode transducer, manufacturing technique, platelet, chemical etching, D-band, Cosmic Microwave Background

# 1 Introduction

In this paper we present a D-band waveguide orthomode transducer (OMT) fabricated with chemically etched brass platelets and evaluate its performance in the context of current and future Cosmic Microwave Background (CMB) polarization measurements.

The CMB is a relic radiation from the early stage of our Universe that is currently detected as a blackbody spectrum with a brightness peak around 160 GHz [1] and it has proven to be a powerful tool to constrain the cosmological parameters to sub-percent precision [2]. About 10% of the CMB intensity is linearly polarized. This fraction can be decomposed into two components, the so-called *E*-modes and *B*-modes [3]. The *E*-modes are due to both scalar (plasma density) fluctuations and tensor (gravitational waves) fluctuations in the primordial plasma, while *B*-modes are generated by tensor fluctuations only.

While *E*-modes have been characterized with high precision [4, 5], *B*-modes remain a subject of active research. On small angular scales ( $\lesssim 1^\circ$ ) the dominant source of *B*-modes is the gravitational lensing (GL) that CMB photons experience in the proximity of large structures like galaxies or galaxy clusters. On larger scales the *B*-modes are expected to have been generated by gravitational waves during inflation. While GL *B*-modes have already been measured [6, 7], the “cosmological” fraction remains undetected, primarily due to its extreme faintness, requiring detectors with ultra-high sensitivity as well as with comparable control of systematic effects and astrophysical foregrounds.

Large arrays of antennas coupled to polarization dividers, ultra-low noise detectors, and multi-frequency observations are key factors in reaching the necessary sensitivity to detect the cosmological *B*-modes signal [8]. OMTs are passive polarization dividers that separate incoming radiation into two orthogonal, linearly polarized components and have been widely used in radio astronomy experiments, in the millimeter and sub-millimeter range. Three main types of OMTs can be found in literature: planar, symmetric, or asymmetric waveguide structures.

Planar OMTs are generally made of four metal probes on a substrate (silicon) membrane. This design is often used in modern CMB experiments above 90 GHz, as they are easily scalable to arrays of thousands of elements and, combined with on-chip filters, provide multi-chroic performance [9, 10]. They are usually fabricated by deep-ion etching and require additional on-chip power combiners to be coupled to the detectors. Typically, planar OMTs display return losses (RL)  $< -15$  dB, which is mainly limited by power leakage in the coupling to the antennas. The port isolation is generally  $< -20$  dB, limited by crosstalks between the probes and the detectors within the transmission line.

Waveguide OMTs, symmetric or asymmetric, notably perform better than planar ones. Symmetric OMTs display wider bandwidth (typically 30% – 40%) and good electromagnetic performance (RL  $< -20$  dB, port isolation  $< -40$  dB), though at the expense of a mechanically complex design. Several prototypes have been fabricated using milling [11–14], electroforming [15] or silicon micro-machining [16] up to 500 GHz.

Asymmetric waveguide OMTs, like the one presented in this work, feature a simpler mechanical designs while achieving electromagnetic performance comparable to that of symmetric OMTs at the cost of a narrower bandwidth (less than 20%). They can also be designed for dual-band operation [17, 18]. Several prototypes have been fabricated by milling [19], micro-milling [20], or electroforming [21], reaching frequencies up to 600 GHz.

Although all the aforementioned manufacturing techniques provide tight mechanical tolerance ( $\simeq 30 \mu\text{m}$ ), they are generally either expensive or time-consuming, and therefore not ideal for producing large arrays.

Our work represents the first waveguide OMT manufactured through the combination of chemical etching and the so-called platelet technique. The platelet technique consists of drilling thin metal plates (platelets) that are subsequently stacked, aligned, and clamped to form the desired profile. Chemical etching is a low-cost manufacturing technique that consists of the controlled erosion of metal plates through an acid solution. Since chemical etching permits the drilling of several plates simultaneously with a mechanical tolerance of 50/30  $\mu\text{m}$ , it can be applied to produce large arrays with hundreds of elements. Indeed, it has already proven successful in fabricating corrugated feed-horn arrays with performance comparable to the state-of-the-art up to 150 GHz [22, 23].

We focus on an asymmetric D-band (130 – 170 GHz) OMT intended to be coupled to the central antenna of the 37-element corrugated feed-horns array described in Mandelli et al [22] on one side and to a pair of kinetic inductance detectors (KIDs) on the other. In Section 2 we detail the electromagnetic and mechanical design of the OMT prototype. In Section 3 we show the mechanical measurements of the

thin etched plates assessing the achieved manufacturing tolerance, along with the simulated frequency response based on the measured OMT profile. In Section 4 we present the experimental setup and discuss the measured frequency response. In Section 5 we summarize the main results and discuss possible improvements and future developments.

## 2 OMT Design

### 2.1 Electromagnetic design

The OMT design (similar to that described in D'Arcangelo et al [24]) consists of a main and a side arm (see top-left of Fig. 1). A circular-to-square waveguide transition is followed by a T-junction polarization divider that splits the incoming radiation into two orthogonal, linearly polarized components, each of which propagates in one of the two arms. The main arm is completed with a 3-step transition to the output, rectangular waveguide. The side arm has a  $90^\circ$  H-bend that rotates the radiation parallel to the main axis, towards a step transition to the output, rectangular waveguide, such that the two output ports lie on the same plane. The intermediate square waveguide limits the bandwidth to around 25%, because the cut-off frequency of the first mode is  $\sqrt{2}$  times that of the fundamental mode, rather than twice the value as in rectangular waveguides.

We modeled and optimized the OMT design using the transient, time domain, solver of the CST Microwave Studio Suite, an electromagnetic simulator based on the Finite Integration Technique (FIT)<sup>1</sup>.

#### 2.1.1 Platelet design

We designed the OMT considering the mechanical constraints detailed in Table 1, specifically:

1. the plate thickness of 0.15 mm was required to ensure a mechanical tolerance of  $\pm 30 \mu\text{m}$  obtained by chemical etching. This implied that the thickness of each OMT component had to be a multiple of this value, as shown in the bottom-left panel of Fig. 1;
2. the circular waveguide diameter and the center-to-center distance between the two output ports were fixed to 1.7 mm and 4.22 mm, respectively, to enable coupling between the OMT, a pre-existing antenna, and two KID detectors on the focal plane;
3. the dimensions of the output waveguides conform to the standard rectangular waveguide dimensions for the D-band.

Additionally, the waveguides have rounded edges, with a radius varying from 0.5 mm to 0.15 mm, since chemical etching does not allow to obtain sharp corners.

We designed each component individually, through a parametric optimization process that fine-tuned the cavity dimensions to meet the performance requirements. In our case, we minimized the return loss across the 130 – 170 GHz band, with a  $-20 \text{ dB}$  requirement at the center of the band. We further optimized the design to ensure a port isolation below  $-50 \text{ dB}$ . The top-right panel of Fig. 1 displays the optimized performance of the input transition, the T-junction, and the H-bend.

**Table 1** Mechanical constraints for the OMT design

Parameter	Requirement
Plate thickness	0.15 mm
Circular waveguide diameter	1.7 mm
Rectangular waveguide major axis	1.65 mm
Rectangular waveguide minor axis	0.8 mm
Center-to-center rectangular waveguides distance	4.221 mm
Rounded corners radius	0.15 – 0.5 mm

#### 2.1.2 Closure plates

We designed our prototype to be mechanically clamped, a process that eliminates the need for glue or bonding, allowing for disassembly and replacement of individual plates, if needed. The platelets are

<sup>1</sup><https://www.3ds.com/products/simulia/cst-studio-suite>

stacked between 5 mm thick top plate (housing the 1.7 mm circular waveguide) and three 2 mm thick bottom plates (containing the output rectangular waveguides), which provide the necessary structural stiffness. We designed the closure plates to be manufactured through CNC milling since they are too thick for chemically etching.

The radius of curvature of the output waveguides is 0.4 mm, which does not match that of the last platelet (0.15 mm). This mismatch arises because 0.4 mm is the radius of the smallest tool that could mill a 2 mm plate without breaking. As a result, the output waveguides have an oval shape, as shown in the bottom-right panel of Fig. 1.

### 2.1.3 Nominal frequency response

In the nominal case of a perfect electric conductor (PEC) material and a perfect geometrical profile without the closure plates we obtain the simulated frequency response displayed in Fig. 2. For each arm, we report the scattering parameters related to return loss (RL), transmission (T), and isolation (I) coefficients. We specify that, throughout this paper, we define the return loss as:  $RL = 10 \log_{10} |S_{11}|^2$ .

The nominal case features  $RL < -10$  dB over most of the 130 – 170 GHz range and  $< -20$  dB at the center of the band. The port isolation is less than  $-80$  dB and transmission is close to 0 dB. Adding the closure plates does not significantly alter the expected performance. Finally, we simulated the OMT response assuming the true materials, a combination of brass and aluminum, as further discussed in Section 2.2: due to the finite conductivity of the materials, the more realistic expected transmission is around  $-0.5$  dB. We call this case *trade-off* design and we will assume this configuration in the rest of the paper.

## 2.2 Mechanical design

The top row of Fig. 3 displays the prototype front and rear views, whereas the bottom-left panel shows a 3D-printed mockup of the OMT profile inside the metal structure.

We designed our OMT to be coupled to the central antenna of a preexisting feed-horn array, described in Mandelli et al [22], to illuminate a KID focal plane. The feed-horn system consists of 37 corrugated feed-horns distributed with a center-to-center distance of 11 mm on a hexagonal footprint of 49 mm side. Our prototype shares the same hexagonal geometry and consists of 62 thin brass plates of 0.15 mm thickness overlapped between a 5 mm thick top plate and a 2 mm bottom plate, both made of aluminum. Each plate also contains two holes for the 2 mm dowel pins, 17 M2 and six M4 screw holes for the mechanical alignment and clamping. The CAD design of a thin plate is shown in the bottom-center panel of Fig. 3.

The prototype is completed by two additional, twin bottom plates of 2 mm thickness, hosting the same oval output waveguides and screw holes of the first bottom plate, but with a custom outer trench to interface with the focal plane. The CAD design of this last bottom plate is shown in the bottom-right panel of Fig. 3. Since the trench is in line with the OMT dowel pins, we inserted three additional pin holes in each of the three bottom plates to align them together. We used the last, 2 mm thick, interface plate to host the screw heads and we used the thicker top plate to tighten the screws, as well as place the dowel pins and guarantee their orthogonality to the plates during the assembly.

The material and thickness of the thin, intermediate plates have been determined by manufacturing constraints since the chemical erosion of the small structures that constitute our platelet design is guaranteed with a mechanical tolerance of  $\pm 30 \mu\text{m}$  only for 0.15 mm brass plates.

In the context of our explorative study, we chose brass over more lightweight and conductive materials, like aluminum, because of its compatibility with chemical etching. The expected OMT transmission is not significantly different from that of an aluminum counterpart, and could be further improved by silver plating if necessary. Additionally, weight constraints were not critical in our case. However, weight could become a limiting factor in space applications.

A possible downside in the use of brass is the linear expansion coefficient ( $19 \times 10^{-6} \text{ }^{\circ}\text{C}^{-1}$ ) being slightly different from that of aluminum ( $24 \times 10^{-6} \text{ }^{\circ}\text{C}^{-1}$ ), constituting the rest of the receiver. However, the limited dimensions of the devices imply that the difference in contraction between one material and the other at the operating temperature ( $\sim 0.1$  K) is below the mechanical tolerance itself and, therefore, acceptable.

Finally, we note that for thicker plates or more relaxed tolerance constraints, as could be the case for lower-frequency devices, chemical etching could be used on aluminum plates, too.

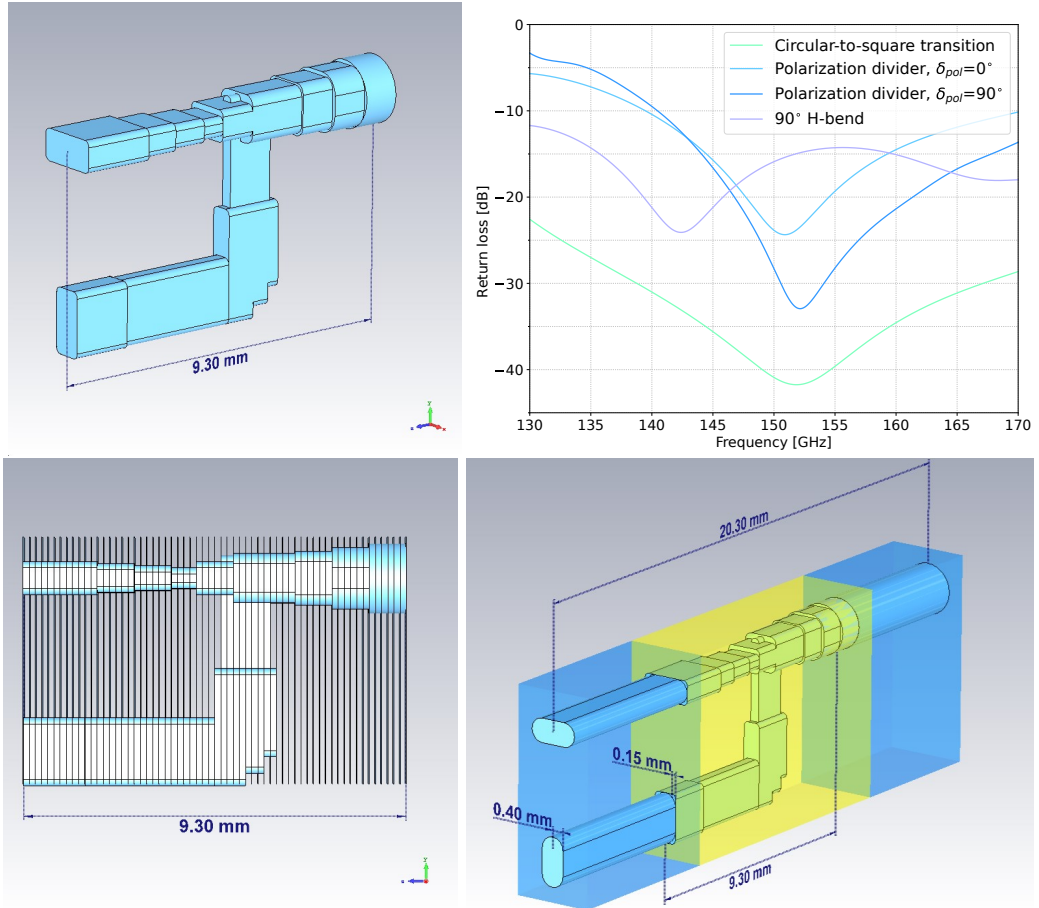


**Fig. 1** *Top-left:* OMT design. The image shows the inner structure, in light blue, where radiation propagates. *Top-right:* optimized performance of the OMT main components. We show the polarization splitter response in the case of horizontal ( $\delta_{\text{pol}} = 0^\circ$ ) and vertical ( $\delta_{\text{pol}} = 90^\circ$ ) incoming polarization. *Bottom-left:* image showing how the OMT can be subdivided into thin slices perpendicular to its axis, represented by the vertical lines, which permits platelet manufacturing. *Bottom-right:* complete, nominal OMT design. The OMT is packed between a circular input waveguide and two oval output waveguides. The colors represent the materials used: the OMT is made of brass (yellow) and the closure plates of aluminum (blue). This is also called *trade-off* design.

### 3 Manufacturing

The thin plates have been chemically etched at Lasertech SRL in Milan, whereas the closure plates have been fabricated at the workshop of our Physics Department. The etching process involves stamping the mechanical design onto a photo-sensitive master layered on a thin metal sheet. This sheet is then exposed to UV radiation, imprinting the design, and subsequently immersed in an acid bath, where the unimpressed material is progressively eroded. The fabrication of the closure plates consists of drilling circular or oval holes by means of a computer numerically controlled (CNC) milling machine.

#### 3.1 Metrological measurements for quality assessment

We performed metrological measurements of all the plates using our Werth ScopeCheck 200 machine, shown in Fig. 4, to asses the achieved fabrication precision against the maximum achievable tolerance. The mechanical tolerance of the chemical etching is  $\pm 0.03$  mm on 0.15 mm thick brass plates, whereas the CNC milling precision is  $\pm 0.03$  mm. Six plates were etched from the same metal sheet, so that from 11 sheets we obtained 66 plates of which 62 were used in the assembly and 4 were considered as spares.

For each pin hole and OMT profile, we measured its dimensions (diameter or rectangular axes) and the  $x$ , and  $y$  center coordinates, comparing them to their nominal value. In the case of circular profiles, we also measured the deviation from circularity (form tolerance, FT<sup>2</sup>). FT measurements are sensitive

<sup>2</sup>The form tolerance of a round shape is the width of the annular ring containing the shape.

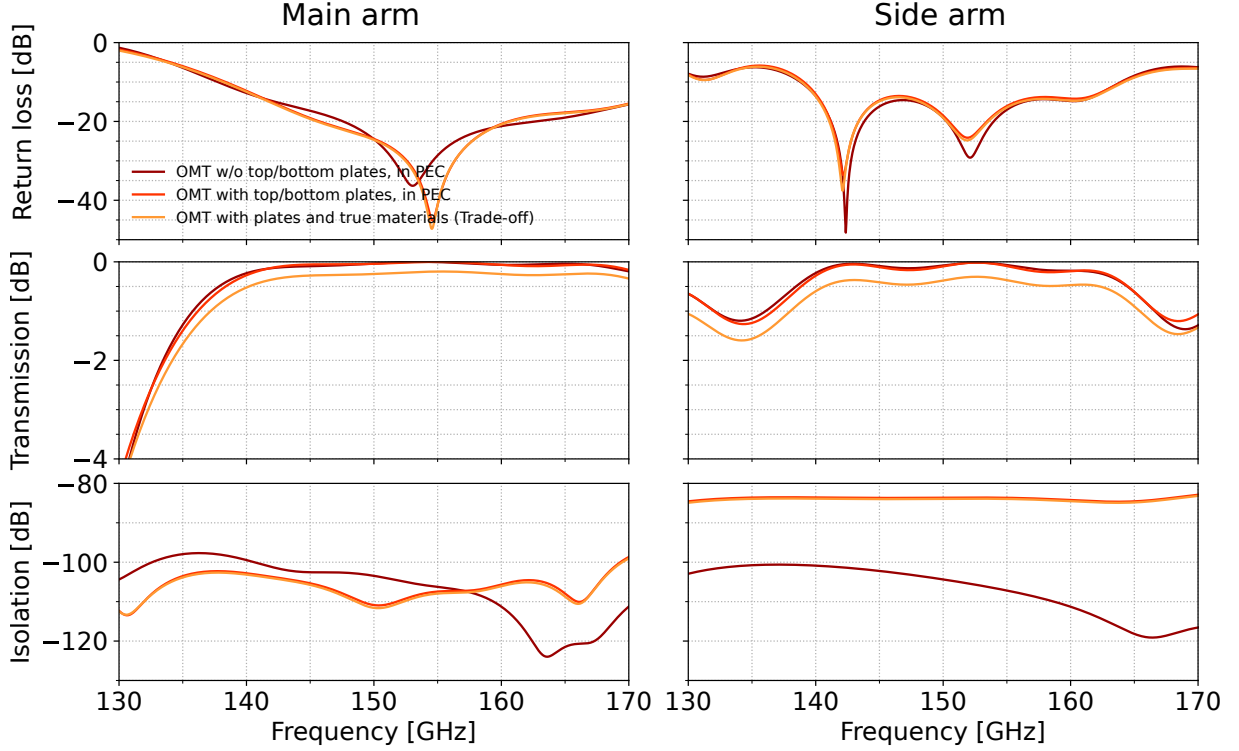


**Fig. 2** Simulated, nominal scattering parameters. The dark-red curves represent the nominal OMT without closure plates, assuming PEC material. The OMT completed with the closure plates is plotted in red, assuming PEC. The transition from the rectangular to the oval output does not significantly alter the performance. The same OMT, but assuming the real manufactured materials, brass, and aluminum, is plotted in orange. The transmission due to the finite conductivity of the materials is around  $-0.5$  dB.

to any shavings or impurities along the measured profile but, according to our experience in fabricating chemically etched feedhorn arrays, a  $FT < 10 \mu\text{m}$  indicates no significant deviation from circularity.

The measurement of the rectangular profiles could not be completely automatized and this made it more prone to systematic errors introduced by the operator. We checked these measurements for each platelet by comparing the deviations of the alignment pin center positions with the deviations of the rectangular profiles and verified that both were consistently less than about  $10 \mu\text{m}$ .

Figure 5 shows the measurements of one of the two pin holes and of the OMT main arm. Similar results were obtained for the other pin and the OMT side arm, but are not shown here to avoid redundancy. The  $\pm 6 \mu\text{m}$  error bar is the metrological machine intrinsic uncertainty.

The  $x$  and  $y$  center coordinates comply with the mechanical tolerance and show a systematic shift towards positive deviations: the measurements are closely scattered around an average value of  $\Delta x = (5 \pm 6) \mu\text{m}$ ,  $\Delta y = (17 \pm 6) \mu\text{m}$  for the pins and  $\Delta x = (9 \pm 6) \mu\text{m}$ ,  $\Delta y = (7 \pm 6) \mu\text{m}$  for the OMT. The pin diameters also comply with the mechanical tolerance, with a few outliers, and the  $FT$  is on average below  $10 \mu\text{m}$ , showing no significant deviation from circularity.

Most of the major and minor axes are slightly out of spec. Since the results are consistent with the pin measurement within  $10\text{--}20 \mu\text{m}$ , we exclude the possibility that this discrepancy arises from an error in our measurement strategy. Instead, we attribute it to the erosion rate: by the time the acid had fully eroded the 2 mm pinhole, it had already over-eroded the OMT profile, whose nominal dimensions are slightly smaller than those of the pin.

The grey areas in the bottom panels of Fig. 5 represent measurements of the minor axis of the polarization divider. This measurement was particularly challenging due to the presence of rounded corners within the T-junction, which may have introduced systematic uncertainties not accounted for by the error bars shown in the graphs.

Overall, all the measurements are systematically larger than their nominal value, especially those of a group of 6 plates (1 sheet) after the polarization division (orange points). This over-erosion results from the limited control of the erosion process and has been noticed in our previous work on feed-horn arrays

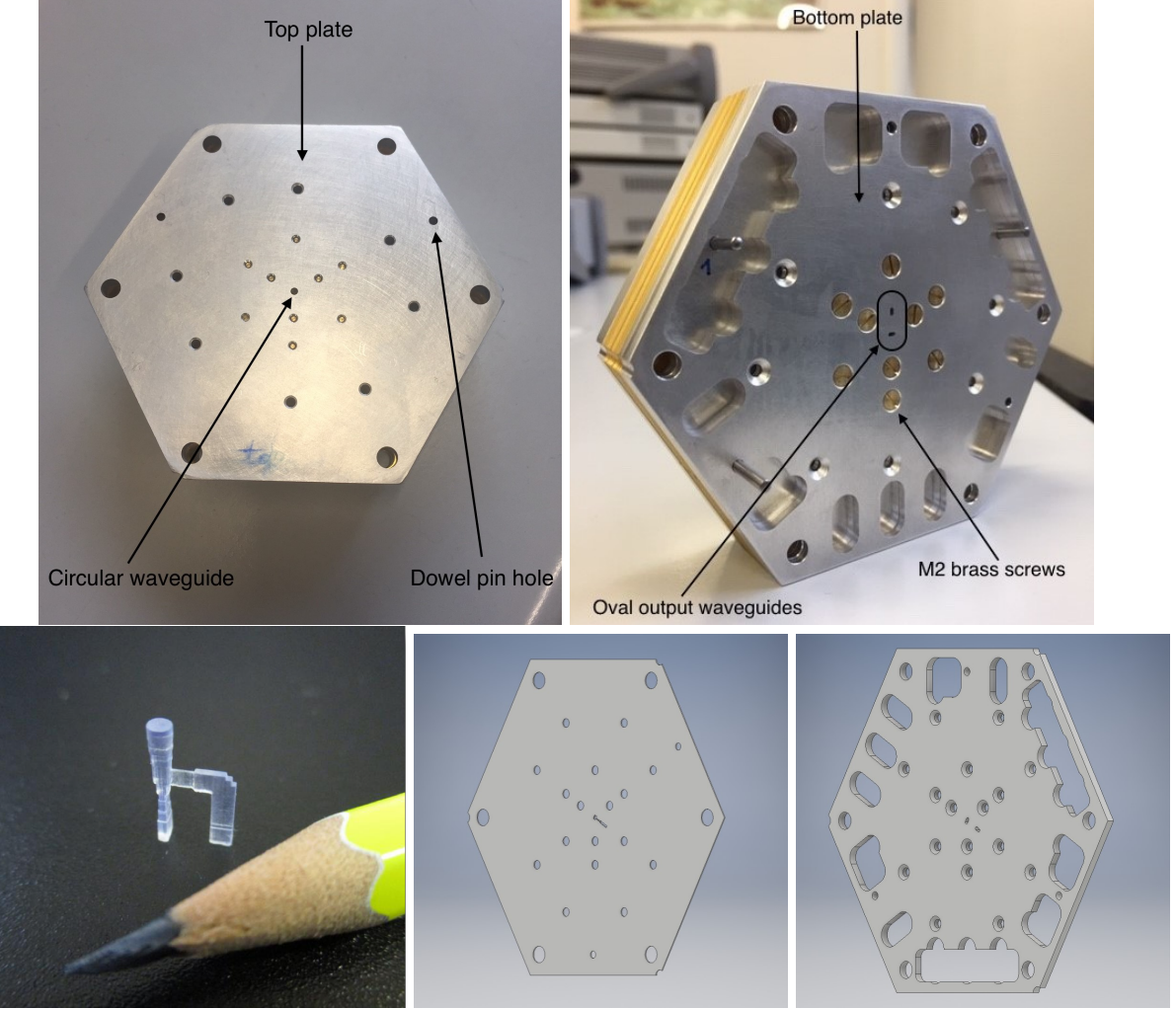


**Fig. 3** *Top row:* Front and rear view of the OMT. *Bottom row:* 3D-printed mockup of the inside of the OMT (left), design of a thin, intermediate plate (center), and one of the bottom plates with the custom outer trench (right).

[22, 23]. We discuss the effects of these systematic deviations on the OMT performance in Section 3.2, where we show that the six plates with the largest deviation do not degrade the simulated response significantly, which led to the choice not to substitute them. Moreover, the over-erosion measurements allow us to compensate for this systematic effect in future prototypes by properly rescaling the dimensions in the mechanical design.

The measurements of the closure plates comply with the milling mechanical precision and are omitted for simplicity.

The array was manually aligned using two orthogonal grinded surfaces and rectified steel dowel pins. We tightened the OMT using M2 brass screws and qualitatively checked the alignment of the first plates with our Werth machine. We used the seven inner screws to clamp the OMT, so that the remaining M2 screws can be used to couple the OMT to the feed-horn array and the M4 screws to couple the overall system to its focal plane.

### 3.2 Simulations including fabrication systematic effects

We performed electromagnetic simulations on a model OMT based on the measured profile to assess the performance reduction caused by imperfections and misalignments introduced during the assembly. We explain the strategy that allowed us to reconstruct and simulate the measured profile in Section 3.2.1 and show the results of the electromagnetic simulations in Section 3.2.2.

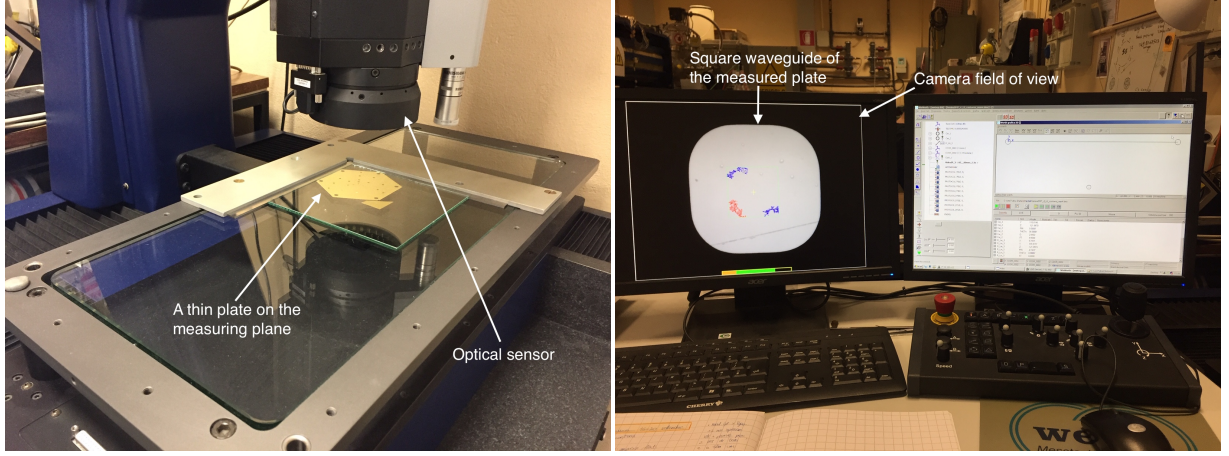


**Fig. 4** *Left panel:* Werth ScopeCheck 200 metrological machine measuring one of the thin plates. *Right panel:* Machine control monitors and console.

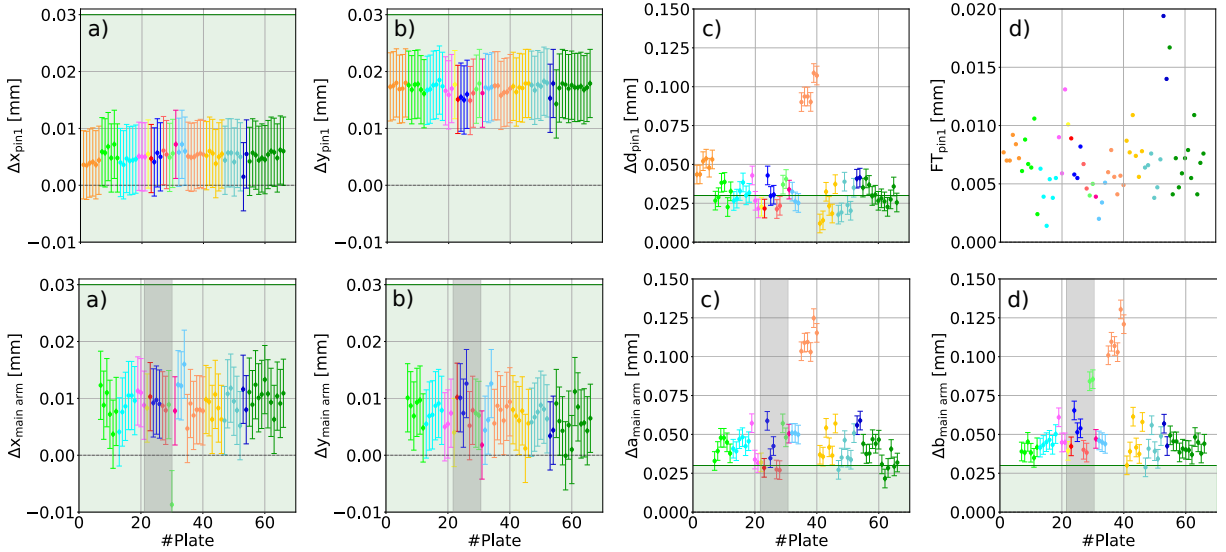


**Fig. 5** *Top row:* Metrological measurements of one of the two pin holes. Deviation,  $\Delta$ , between measured and nominal:  $x$  (a) and  $y$  (b) center coordinates, diameter  $d$  (c), and measured FT (d), which indicates a deviation from circularity. *Bottom row:* Metrological measurements of the main arm. Deviation between measured and nominal:  $x$  (a) and  $y$  (b) center coordinates, major waveguide axis  $a$  (c), and minor waveguide axis  $b$  (d). Measurements of the same color belong to the same section of the OMT (e.g. dark green for the rectangular waveguide plates). The green area highlights the expected manufacturing tolerance,  $\pm 30 \mu\text{m}$ , while the grey area highlights the plates forming the polarization divider, which were difficult to measure and could be overestimated. Note that, since we are showing the square and rectangular waveguide of the main arm, the first six plates containing the circular waveguide are missing.

### 3.2.1 Metrological point-cloud acquisition

We performed a *point-cloud acquisition* on each plate using our Werth metrological machine, which consists of the semi-automatic motion of the optical sensor along the OMT profile and the simultaneous measurement of the point coordinates, in the machine  $x$ - $y$  reference frame, with a fixed sampling (around 50 pts/mm). The points are saved in a text file, thus allowing us to reconstruct the measured profile *a posteriori*, as shown in the example in the top-panel of Fig. 6. We imported the datasets into CST Microwave Studio to reconstruct the 3D model of the measured OMT, as can be seen in Fig. 7, which contains the manufacturing defects and systematic effects both in the geometry and position of the platelets.

In the CST model we used a coarser mesh compared to the measurement resolution of 50 points per mm in order to maintain the total number of cells within  $\sim 2 \times 10^6$ , which was compatible with the available computing resources.

With the measured data we simulated three cases:

- A. the OMT with the measured profile;
- B. an OMT in which we shifted all the measured profiles in the origin of the coordinate system to simulate the over-eroded, but aligned cavities;
- C. as in case B with a random misalignment in the cavity centers to study the sensitivity to a plate-to-plate misalignment induced during the mechanical assembly.

Case C was particularly interesting as mechanical misalignment is a well-known cause of performance reduction in waveguide OMTs [13]. In our case, although we used two orthogonal grinded surfaces as support during the assembly process, some level of plate misalignment could still arise from the pin holes accuracy.

To study the sensitivity of our prototype to this effect, we added a  $(\Delta x, \Delta y) = (\Delta r \cos \theta, \Delta r \sin \theta)$  to the measured position of each plate, where  $\theta$  is randomly distributed between  $[0, 2\pi]$  and  $\Delta r$  is randomly sampled from a Gaussian distribution centered around  $\mu = 0$  mm, with  $\sigma$  equal to the mean pin radius deviation ( $\sigma = 0.019$  mm). This represents the situation in which the OMT is assembled along the input waveguide axes (distribution centered in  $\Delta r = 0$  mm) with a plate-to-plate misalignment.

### 3.2.2 Simulated electromagnetic performance

Figure 8 compares the simulations of the measured OMT, the measured and aligned OMT, and the nominal (trade-off) design. As expected, the manufacturing systematic effects degrade the OMT's performance, particularly the return loss and isolation. However, the degradation is primarily attributed to the discontinuity between plates and the systematic effects in the geometry of the profiles, rather than their positions.

Nonetheless, the return loss remains below  $-10$  dB in the  $140 - 160$  GHz range and below  $-20$  dB at the center of the bandwidth. The transmission coefficient is approximately  $-0.5$  dB in the same range, and the isolation remains below  $-30$  dB across the entire bandwidth. The results also demonstrate that as long as the plates are properly aligned along the circular waveguide axes, the accuracy of the etched pin holes does not significantly affect the OMT performance.

## 4 Electromagnetic measurements

In this section, we present the electromagnetic measurements that were carried out at the Physics Department of the University of Milano-Bicocca. In particular, we describe the instrumental setup used to measure the frequency response of the OMT prototype, we present the measured scattering parameters and discuss the transmission and isolation results.

### 4.1 Measurement setup and "shorted" method

The OMT is connected to a vector network analyzer (VNA) by means of two frequency multipliers: a transmitter (TX head), that multiplies the low-frequency signal of the VNA ( $10 - 20$  GHz) to high-frequency, and a receiver (RX head) that down-converts the high-frequency signal leaving the OMT to low frequency back into the VNA. The setup is shown in Fig. 9. We used two OML millimeter extensions (model V06VNA2-T/R-A) for full 2-port S-matrix characterization in the  $110 - 170$  GHz band and an Agilent PNA-X VNA (model N5246A). We calibrated the system using a 2-port TRL (Thru-Reflection-Line) calibration kit from OML.

The TX and RX heads interface with the OMT through a rectangular waveguide with a standard UG387/U-mod flange. However, none of the OMT top and bottom flanges can interface to a standard flange. We, therefore, used two additional flanges (top and bottom) that extend the OMT port with either a circular or an oval waveguide and that can be screwed to the OMT on one side and interface to the standard flange on the other. A circular-to-rectangular transition is screwed onto the top flange to interface with the TX head.

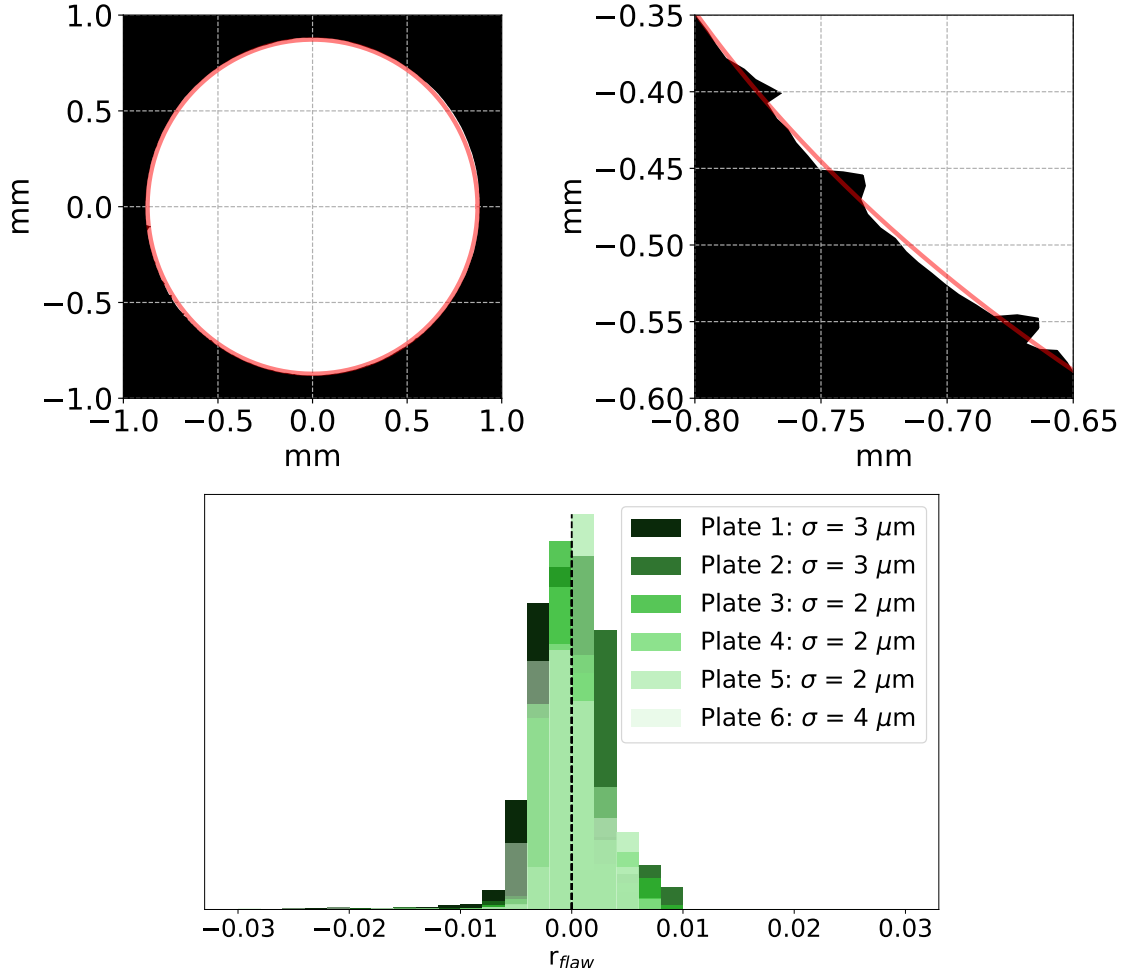


**Fig. 6** *Top panel:* Example of a reconstructed OMT plate using the point-cloud acquisition. We show the first 0.15 mm plate, containing the circular waveguide, on the left. The metal plate is black and the cavity is white. The red circle is the best fit, obtained from the measured diameter. A close-up of the same plate is shown on the right, highlighting the details of the reconstructed profile, including the flaws and imperfections along the etched waveguide. *Bottom panel:* distribution of the etching roughness,  $r_{\text{flaw}}$ , for the six OMT plates containing the circular waveguide, quantified as the deviation of the radius given by the measured  $x$  and  $y$  point coordinates from the metrological best-fit radius. The distributions are centered in zero, with a tail at negative  $r_{\text{flaw}}$  due to the bumps along the etched profile, and with a RMS  $\simeq 3 \mu\text{m}$ .

Conventionally, the scattering parameters are measured ensuring impedance matching along the waveguide chain. During reflection measurements, the OMT input port is connected to the TX head, which transmits the signal and receives it back, while each OMT output port is terminated with a load that absorbs any transmitted radiation. During transmission and isolation measurements, the input and one of the output ports are connected to the TX and RX heads, respectively, while the port not under test is terminated with a load.

However, the two output ports of our OMT are too close to each other to simultaneously connect them both to a standard flange (load or extension), since their center-to-center distance is only 4.22 mm. Therefore, we used a slightly different experimental setup: we fabricated the bottom flange with only one oval waveguide, so that it connects the port under test to the measurement chain (the RX head or a load) and, at the same time, the metal part blocks the other output port. The radiation coming to the port not under test is thus reflected, instead of absorbed, and creates stationary waves inside its arm. We call this method *shorted*.

To compare the performance of the shorted method with the rigorous, adapted one, we simulated the measurement in CST with both methods. Figure 10 compares the two simulated responses and shows that reflection and transmission curves essentially overlap. During isolation measurements, instead, the stationary waves form in the arm that is aligned with the incoming polarization and, therefore, receive

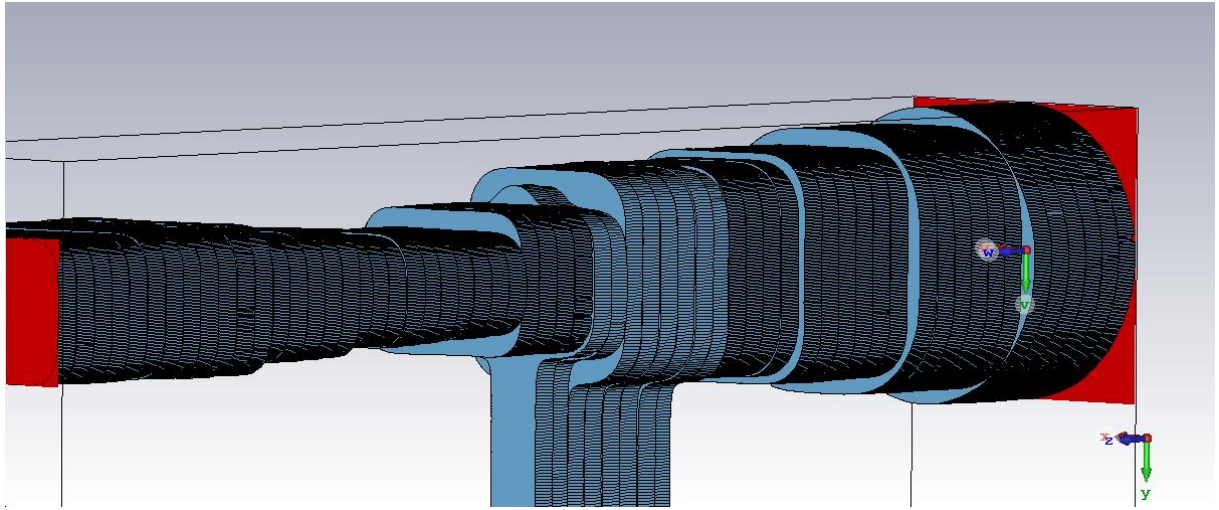


**Fig. 7** Close-up on the 3D model of the manufactured OMT reconstructed from the metrological data.

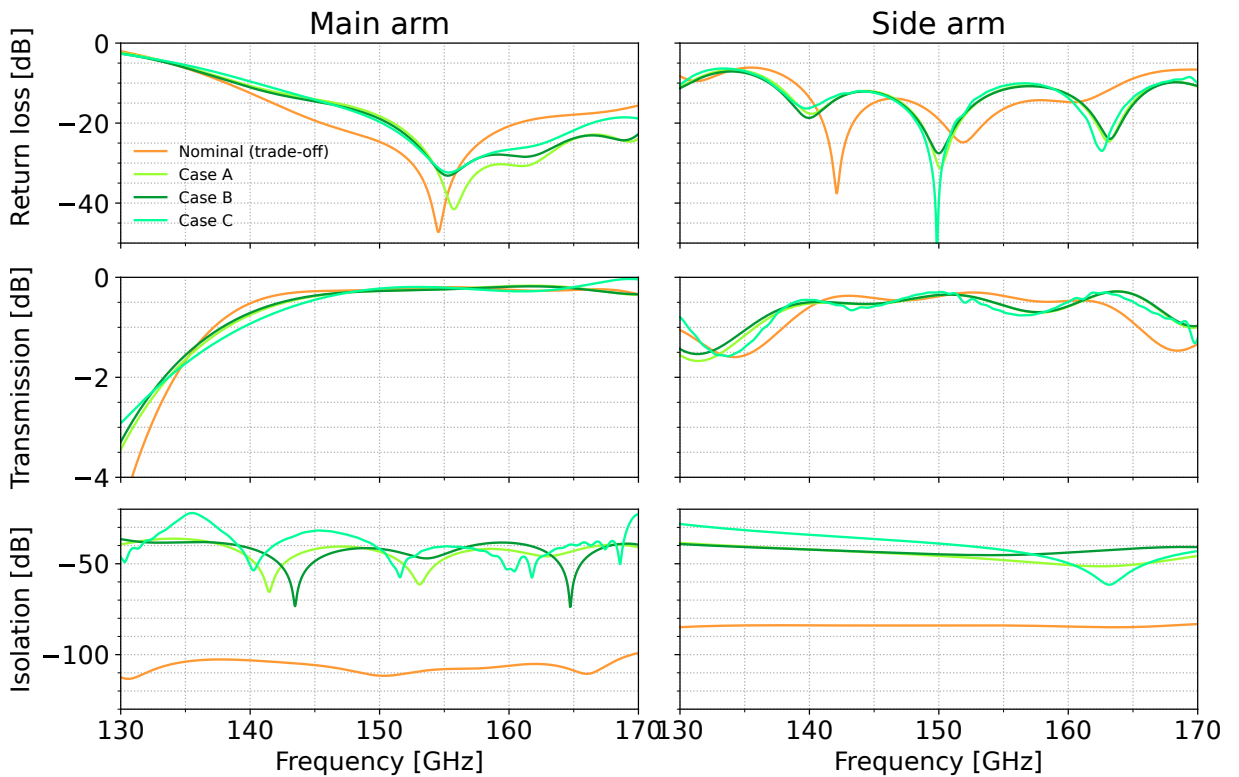


**Fig. 8** Comparison of simulated performance. *Orange*: nominal (trade-off) case; *light green*: case A (profile with measured data); *dark green*: case B (measured profile with aligned centers); *light blue*: case C (case B with random misalignments). The OMT performance is mainly altered by the discontinuities of the over-etched profile.

the majority of the signal. Part of the stationary signal is transmitted back into the arm under test and generates the resonances that are visible in the isolation plot. Nevertheless, the average value sets at a level below  $-30$  dB. These results confirm the applicability of the shorted method to measure the OMT electromagnetic performance.

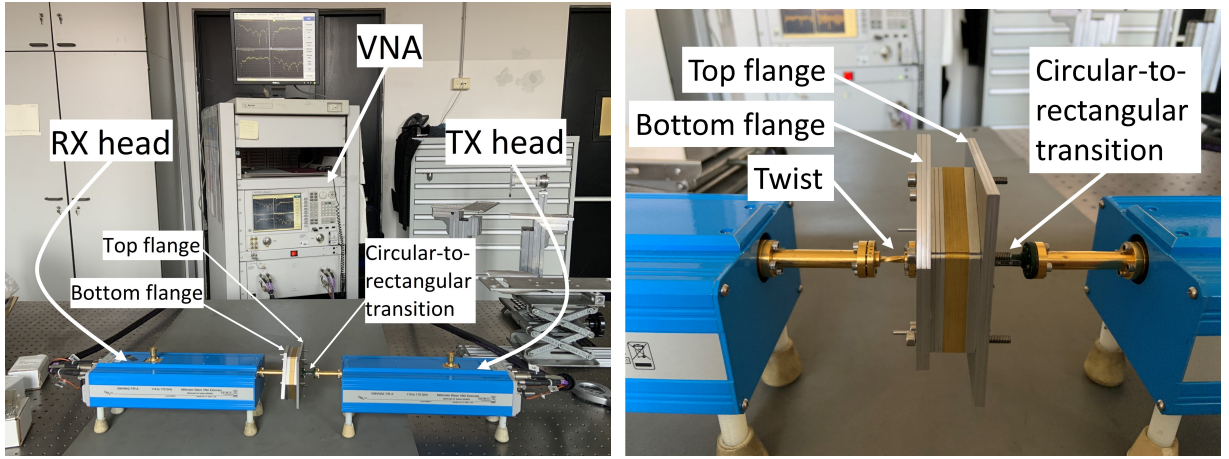


**Fig. 9** Experimental setup. *Left panel*: the transmission line. The OMT is connected to the TX frequency multiplier through a flange and a circular-to-rectangular transition on the right, and to the RX frequency multipliers on the left, through a second flange that simultaneously blocks the output port not under test. The rectangular waveguides of the TX and RX heads are coherently aligned and powered by the VNA in the back. *Right panel*: the isolation measurement. The measured output port is the one rotated by 90° with respect to the incoming TX radiation and is connected to the RX head through a 90° twist.

## 4.2 Results

Figure 11 compares the measured and expected scattering parameters. The measured return loss is below  $-10$  dB over the  $140 - 160$  GHz range and below  $-20$  dB at the center of the bandwidth for both arms. Overall, the curve matches the simulation, even though the resonances are slightly shifted in frequency, especially in the side arm.

The measured transmission is around  $-2$  dB and  $-2.5$  dB for the main and side arm, respectively. The measurement refers to the complete waveguide chain including the OMT and its interfaces (top and bottom flanges plus the transition). To isolate the OMT transmission, we measured the insertion loss (IL) of each interface and subtracted it from the measurement. Specifically, we measured the return loss of the interface terminated with a short and estimated the IL as half the average signal. For the bottom flange, we also measured its transmission and checked that it was compatible with the estimated IL, which confirmed the reliability of our IL measurement strategy.

The total contribution of the interfaces is around  $0.5$  dB. Therefore, the estimated OMT transmission is around  $-1.5$  dB and  $-2$  dB for the two arms, which is more than  $1$  dB larger than the simulation. The fact that the side arm, which is the longer arm in terms of electromagnetic path, has a lower transmission than the main arm suggests that the cause is related to an increase of resistive losses due to surface roughness.

Indeed, surface roughness is a well-known cause of transmission losses in the millimeter range [25–27]. If the frequency is high enough that the skin depth falls below the surface roughness dimension, the imperfections cause extra parasite currents that increase the resistive losses [25]. Because we downgraded the mesh of our reconstructed OMT model (see Section 3.2) our simulations do not properly account for the effects of profile imperfections.

CST allows the simulation of this effect by specifying a parameter, the root mean square (RMS) of the roughness, which is used to compute an effective conductivity and solve the modified field equations, following the gradient model introduced in Gold and Helmreich [25]. We performed the simulation of the reconstructed OMT assuming a value of RMS compatible with the one obtained from the metrological measurements,  $\text{RMS}_{\text{brass}} = 3 \mu\text{m}$ , as indicated by the distribution in the bottom panel of Fig. 6.

The simulation results (displayed in Fig. 11) confirm that this effect can reproduce the average measured transmission, and also causes a slight shift in the frequency of the resonances in the side arm that matches the measurements.

The measured isolation is below  $-20$  dB along the full bandwidth, therefore around  $-10$  dB higher than the simulation. Further simulations suggest that this could be due to a slight polarization angle rotation within the measured setup. Figure 12 shows the comparison between measured and simulated

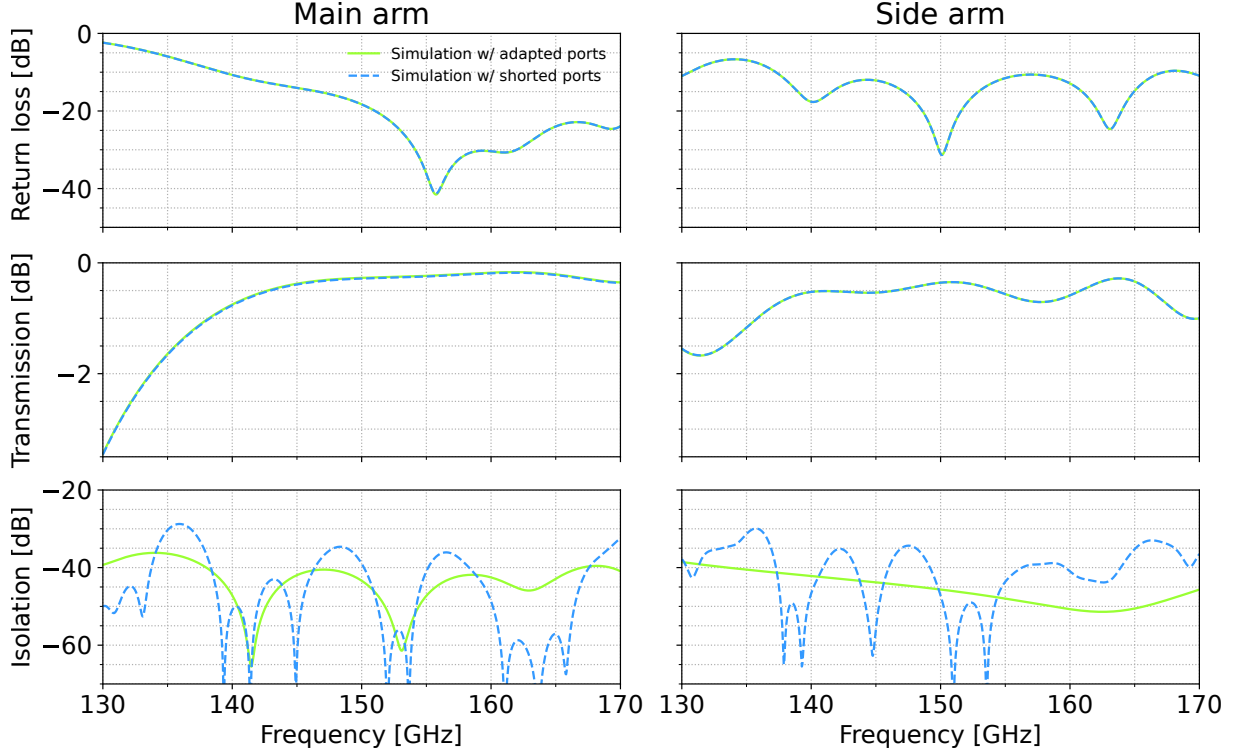


**Fig. 10** The expected performance using our *shorted* measurement setup compared with the true scattering parameters, namely the ones we would expect to measure if we properly adapted the OMT ports. The solid green curve is the metrologically measured OMT, whereas the dashed sky blue curve is the same OMT but with the port not under test blocked out by a metal plate (shorted).

isolation assuming a 1° and 3° rotation and confirms that a 3° rotation would be enough to explain the measured isolation level. We assessed the possible role of the 90° twist that was placed between the output port and the RX head during the isolation measurement by repeating the test without the twist and rotating the RX head around its side. Since we did not observe any difference in the measured isolation, we excluded the twist as the cause, although we could not precisely determine where the rotation occurred along the remaining waveguide chain.

However, we emphasize that even if the measured isolation represents the actual OMT isolation, it remains comparable to the isolation levels of planar OMTs currently used in CMB experiments.

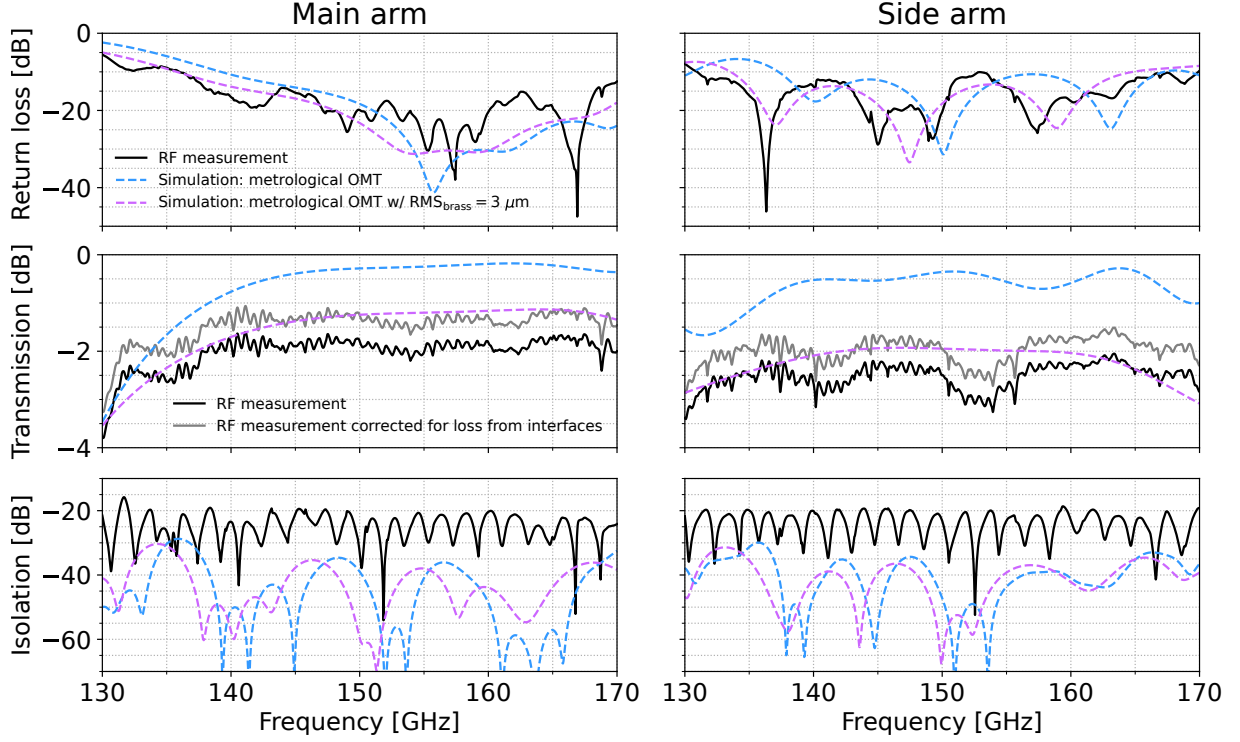
We also checked whether a more conductive material, like aluminum (which is twice as conductive compared to brass), would lead to the same result in case of surface roughness. Therefore we simulated the metrologically measured OMT (case A) assuming completely made of aluminum with and without the same surface roughness considered for brass ( $RMS_{Al} = RMS_{brass} = 3 \mu\text{m}$ ).

Figure 13 compares the simulated transmission for the two cases and confirms that the transmission loss is caused by the surface roughness alone, independently from the material. This result highlights a limit of chemical etching in all the applications in which resistive losses, even of few dB, must be avoided.

## 5 Conclusions

In this paper we presented the design, fabrication, and testing of an asymmetric waveguide OMT working in the D-band (130 – 170 GHz) realized with chemically etched brass platelets that were subsequently aligned and mechanically clamped.

The aim of our study was to investigate fast, low-cost (less than 1 kEuro for this prototype), and scalable manufacturing techniques for producing large arrays of OMTs to be coupled to feed-horn antennas and KIDs arrays for measuring the CMB polarization. We focused on chemical etching in combination with the platelet manufacturing technique, which has already proven successful in producing corrugated feed-horn arrays with state-of-the-art performance up to 150 GHz.



**Fig. 11** The measured performance, in solid black, compared to the expected, simulated one in dashed sky blue, namely, the metrologically measured OMT in the shorted configuration. The transmission measurement includes the OMT and the interfaces: the top and bottom flanges, and the transition. The estimated OMT transmission is shown in solid gray, where we subtracted the measured contribution of the interfaces from the black curve. The dashed purple line is the simulation of the metrologically measured OMT in the shorted configuration, with an additional parameter, the root mean square of the surface roughness, that accounts for the measured flaws along the etched profile, which we set to  $\text{RMS}_{\text{brass}} = 3 \mu\text{m}$ .

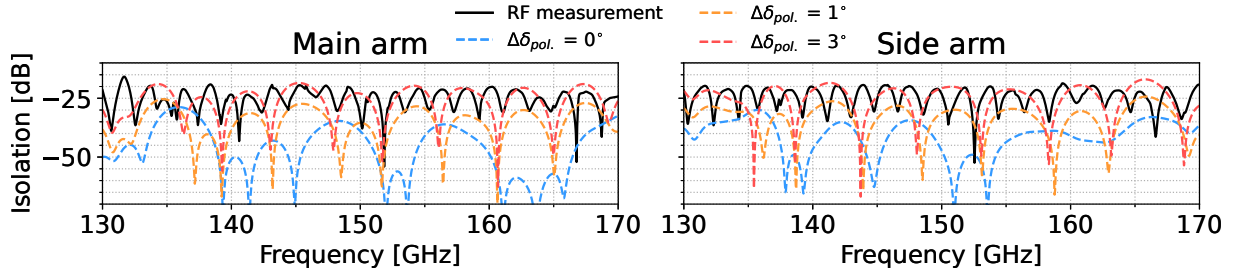


**Fig. 12** Measured and simulated isolation in the case of perfect horizontal or vertical polarization,  $\Delta\delta_{\text{pol.}} = 0^\circ$ , and with a one or three degrees rotation of the polarization angle,  $\Delta\delta_{\text{pol.}} = 1^\circ$  and  $\Delta\delta_{\text{pol.}} = 3^\circ$ , respectively.

We performed both metrological and electromagnetic measurements on our prototype. The metrological tests confirmed a systematic tendency of chemical etching to over-erosion, which was noticed in previous works on feed-horn arrays. This effect can be corrected by properly rescaling the OMT profile during the design phase. Simulations based on the measured profile indicated that the over-erosion mainly degrades the isolation, which increased to around  $-30$  dB, whereas the reflection losses and transmission remained compatible with simulations of the nominal OMT: return loss below  $-10$  dB across the  $140 - 160$  GHz range with a minimum of  $-20/-35$  dB at the center, and transmission above  $-0.5$  dB. The simulations also showed a small sensitivity to plate misalignment that could be induced by the pin holes accuracy during the mechanical assembly.

The measured frequency response showed a return loss compatible with simulations, but with resonances slightly shifted in frequency, a transmission of around  $-1.5/-2$  dB, compared to the expected

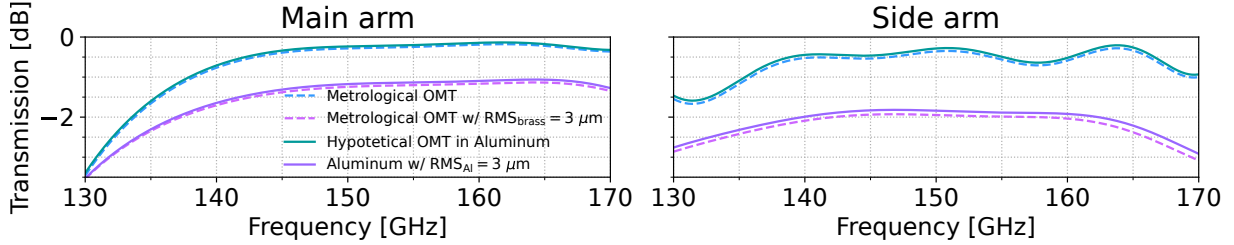


**Fig. 13** Simulated transmission for our metrologically measured OMT made of brass, with and without a root mean square surface roughness equal to the measured one,  $\text{RMS}_{\text{brass}} = 3 \mu \text{m}$ , in dashed purple and dashed blue, respectively. The curves are the same as shown in Fig. 11. The same simulated transmission is shown with solid lines for a hypothetical, identical OMT, but completely made out of aluminum. Using aluminum instead of brass does not improve the loss in transmission if the manufacturing technique leaves imperfections along the OMT profile.

–0.5 dB, and isolation around –20 dB, instead of the expected –30 dB. Further simulations have confirmed that both the transmission and the shift of the resonances can be explained by the surface roughness effect arising from defects along the etched profile ( $\text{RMS} \simeq 3 \mu \text{m}$ ), which is a typical and unavoidable consequence of the chemical erosion.

Further simulations also showed that the increase in the isolation could be explained by a slight rotation of the polarization angle within the measurement chain (around  $3^\circ$ ), even though it was difficult to assess where precisely it could have occurred. Even if this was the actual response of the OMT, it would still be compatible with the isolation of planar OMTs that are currently employed in CMB experiments.

In summary, our study illustrates that chemical etching has the potential to be a fast, low-cost, and scalable technique for producing waveguide OMTs with performance compatible with the state-of-the-art, as long as the OMT design is properly rescaled in the design phase to compensate for the systematic over-erosion of the plates. We have observed a degradation in transmission caused by the roughness of the etched profile, which could limit the applicability of chemical etching to OMTs above 100 GHz for CMB polarization measurements. We believe that chemical etching could still be suitable for lower-frequency OMTs, where the surface roughness should have a smaller impact or for other applications, where an insertion loss of few dB does not represent an issue.

For high-frequency devices, we are currently investigating alternative solutions, like laser micro-machining, that could still guarantee a fast and low-cost production, but with a smoother finish. Our results will be deferred to a dedicated paper.

**Acknowledgements.** This project has been carried out in the framework of the *Kinetic Inductance Detector for Space* and *Premiale* projects funded by the Agenzia Spaziale Italiana (ASI). The authors wish to thank the entire staff of the machine shop at the Physics Department of the University of Milan, for their contribution and key discussions about the realization and assembly process.

## References

- [1] Mather, J.C., Cheng, E., Cottingham, D.A., Eplee Jr, R., Fixsen, D.J., Hewagama, T., Isaacman, R., Jensen, K., Meyer, S.S., Noerdlinger, P.D., *et al.*: Measurement of the cosmic microwave background spectrum by the cobe firas instrument. *The Astrophysical Journal* **420**, 439–444 (1994)
- [2] Aghanim, N., Akrami, Y., Ashdown, M., Aumont, J., Baccigalupi, C., Ballardini, M., Banday, A., Barreiro, R., Bartolo, N., Basak, S., *et al.*: Planck 2018 results-vi. cosmological parameters. *Astronomy & Astrophysics* **641**, 6 (2020)
- [3] Zaldarriaga, M., Seljak, U.: All-sky analysis of polarization in the microwave background. *Physical Review D* **55**(4), 1830 (1997)
- [4] Kovac, J.M., Leitch, E., Pryke, C., Carlstrom, J., Halverson, N., Holzapfel, W.: Detection of polarization in the cosmic microwave background using dasi. *Nature* **420**(6917), 772–787 (2002)
- [5] Crites, A., Henning, J., Ade, P., Aird, K., Austermann, J., Beall, J., Bender, A., Benson, B., Bleem, L., Carlstrom, J., *et al.*: Measurements of e-mode polarization and temperature-e-mode correlation

in the cosmic microwave background from 100 square degrees of sptpol data. *The Astrophysical Journal* **805**(1), 36 (2015)

- [6] Wu, W., Mocanu, L.-M., Ade, P.A., Anderson, A., Austermann, J.E., Avva, J., Beall, J.A., Bender, A., Benson, B.A., Bianchini, F., *et al.*: A measurement of the cosmic microwave background lensing potential and power spectrum from 500 deg<sup>2</sup> of sptpol temperature and polarization data. *The Astrophysical Journal* **884**(1), 70 (2019)
- [7] Ade, P., Akiba, Y., Anthony, A., Arnold, K., Atlas, M., Barron, D., Boettger, D., Borrill, J., Chapman, S., Chinone, Y., *et al.*: A measurement of the cosmic microwave background b-mode polarization power spectrum at sub-degree scales with polarbear. *The Astrophysical Journal* **794**(2), 171 (2014)
- [8] Adam, R., Ade, P.A., Aghanim, N., Akrami, Y., Alves, M., Argüeso, F., Arnaud, M., Arroja, F., Ashdown, M., Aumont, J., *et al.*: Planck 2015 results-i. overview of products and scientific results. *Astronomy & Astrophysics* **594**, 1 (2016)
- [9] Anderson, A., Ade, P., Ahmed, Z., Austermann, J., Avva, J., Barry, P., Thakur, R.B., Bender, A., Benson, B., Bleem, L., *et al.*: Spt-3g: A multichroic receiver for the south pole telescope. *Journal of Low Temperature Physics* **193**(5), 1057–1065 (2018)
- [10] McMahon, J., Beall, J., Becker, D., Cho, H.M., Datta, R., Fox, A., Halverson, N., Hubmayr, J., Irwin, K., Nibarger, J., Niemack, M., Smith, H.: Multi-chroic feed-horn coupled tes polarimeters. *Journal of Low Temperature Physics* **167**(5–6), 879–884 (2012) <https://doi.org/10.1007/s10909-012-0612-9>
- [11] Narayanan, G., Erickson, N.: Full-waveguide band orthomode transducer for the 3 mm and 1 mm bands. In: *Proceedings of the 14th International Symposium on Space Terahertz Technology*, pp. 508–512 (2003)
- [12] Navarrini, A., Bolatto, A., Plambeck, R.L.: Test of 1 mm band turnstile junction waveguide orthornode transducer. In: *Proc. 17th Int. Symp. STT*, pp. 99–102 (2006)
- [13] Navarrini, A., Groppi, C., Lin, R., Chattopadhyay, G.: Test of a waveguide orthomode transducer for the 385–500 ghz band. In: *22nd International Symposium on Space Terahertz Technology 2011, ISSTT 2011*, pp. 99–102. *International Symposium on Space Terahertz Technology*, ??? (2011). *22nd International Symposium on Space Terahertz Technology 2011, ISSTT 2011* ; Conference date: 25-04-2011 Through 28-04-2011
- [14] Pisano, G., Pietranera, L., Isaak, K., Piccirillo, L., Johnson, B., Maffei, B., Melhuish, S.: A broadband wr10 turnstile junction orthomode transducer. *Ieee microwave and wireless components letters* **17**(4), 286–288 (2007)
- [15] Asayama, S., Kamikura, M.: Development of double-ridged waveguide orthomode transducer for the 2 mm band. *Journal of Infrared, Millimeter, and Terahertz Waves* **30**(6), 573–579 (2009)
- [16] Gomez-Torrent, A., Shah, U., Oberhammer, J.: Compact silicon-micromachined wideband 220–330-ghz turnstile orthomode transducer. *IEEE Transactions on Terahertz Science and Technology* **9**(1), 38–46 (2018)
- [17] El Kamili, A., Tribak, A., Terhzaz, J., Mediavilla Sánchez, Á., *et al.*: A dual band orthomode transducer in k/ka bands for satellite communications applications (2018)
- [18] Leal-Sevillano, C.A., Tian, Y., Lancaster, M.J., Ruiz-Cruz, J.A., Montejo-Garai, J.R., Rebollar, J.M.: A micromachined dual-band orthomode transducer. *IEEE transactions on microwave theory and techniques* **62**(1), 55–63 (2013)
- [19] Dunning, A., Srikanth, S., Kerr, A.: A simple orthomode transducer for centimeter to submillimeter wavelengths. In: *Proc. 20th Int. Symp. Space Terahertz Technol.*, pp. 191–193 (2009)

[20] Reck, T.J., Chattopadhyay, G.: A 600 ghz asymmetrical orthogonal mode transducer. *IEEE microwave and wireless components letters* **23**(11), 569–571 (2013)

[21] D’Arcangelo, O., Simonetto, A., Figini, L., Pagana, E., Villa, F., Pecora, M., Battaglia, P., Bersanelli, M., Butler, R., Garavaglia, S., *et al.*: The planck-lfi flight model ortho-mode transducers. *Journal of Instrumentation* **4**(12), 12005 (2009)

[22] Mandelli, S., Manzan, E., Mennella, A., Cavaliere, F., Viganò, D., Franceschet, C., Bernardis, P., Bersanelli, M., Castellano, M.G., Coppolecchia, A., al.: A chemically etched corrugated feed-horn array for d-band cmb observations. *Experimental Astronomy* (2021) <https://doi.org/10.1007/s10686-021-09698-9>

[23] Cavaliere, F., Mennella, A., Zannoni, M., Battaglia, P., Battistelli, E.S., de Bernardis, P., Burke, D., D’Alessandro, G., de Petris, M., Franceschet, C., Grandsire, L., Hamilton, J.-C., Maffei, B., Manzan, E., Marnieros, S., Masi, S., O’Sullivan, C., Passerini, A., Pezzotta, F., Piat, M., Tartari, A., Torchinsky, S.A., Viganò, D., Voisin, F., Ade, P., Alberro, J.G., Almela, A., Amico, G., Arnaldi, L.H., Auguste, D., Aumont, J., Azzoni, S., Banfi, S., Baù, A., Bélier, B., Bennett, D., Bergé, L., Bernard, J.-P., Bersanelli, M., Bigot-Sazy, M.-A., Bonaparte, J., Bonis, J., Bunn, E., Buzzi, D., Chanial, P., Chapron, C., Charlassier, R., Cobos Cerutti, A.C., Columbro, F., Coppolecchia, A., de Gasperis, G., de Leo, M., Dheilly, S., Duca, C., Dumoulin, L., Etchegoyen, A., Fasiczewski, A., Ferreyro, L.P., Fracchia, D., Gamboa Lerena, M.M., Ganga, K.M., García, B., García Redondo, M.E., Gaspard, M., Gayer, D., Gervasi, M., Giard, M., Gilles, V., Giraud-Heraud, Y., Gómez Berisso, M., González, M., Gradziel, M., Hampel, M.R., Harari, D., Henrot-Versillé, S., Incardona, F., Jules, E., Kaplan, J., Kristukat, C., Lamagna, L., Loucatos, S., Louis, T., Marty, W., Mattei, A., May, A., McCulloch, M., Mele, L., Melo, D., Montier, L., Mousset, L., Mundo, L.M., Murphy, J.A., Murphy, J.D., Nati, F., Olivieri, E., Oriol, C., Paiella, A., Pajot, F., Pastoriza, H., Pelosi, A., Perbost, C., Perciballi, M., Piacentini, F., Piccirillo, L., Pisano, G., Platino, M., Polenta, G., Prèle, D., Puddu, R., Rambaud, D., Rasztoky, E., Ringegni, P., Romero, G.E., Salum, J.M., Schillaci, A., Scóccola, C.G., Scully, S., Spinelli, S., Stankowiak, G., Stolpovskiy, M., Supanitsky, A.D., Therneau, J.-P., Timbie, P., Tomasi, M., Tucker, C., Tucker, G., Vittorio, N., Wicek, F., Wright, M., Zullo, A., QUBIC Collaboration: QUBIC VII: The feedhorn-switch system of the technological demonstrator. *Journal of Cosmology and Astroparticle Physics* **2022**(4), 040 (2022) <https://doi.org/10.1088/1475-7516/2022/04/040> arXiv:2008.12721 [astro-ph.IM]

[24] D’Arcangelo, O., Simonetto, A., Figini, L., Pagana, E., Villa, F., Pecora, M., Battaglia, P., Bersanelli, M., Butler, R.C., Garavaglia, S., Guzzi, P., Mandolesi, N., Sozzi, C.: The planck-lfi flight model ortho-mode transducers. *Journal of Instrumentation* **4**(12), 12005 (2009) <https://doi.org/10.1088/1748-0221/4/12/T12005>

[25] Gold, G., Helmreich, K.: A physical model for skin effect in rough surfaces. In: 2012 7th European Microwave Integrated Circuit Conference, pp. 631–634 (2012)

[26] Gold, G., Helmreich, K.: Surface impedance concept for modeling conductor roughness. In: 2015 IEEE MTT-S International Microwave Symposium, pp. 1–4 (2015). <https://doi.org/10.1109/MWSYM.2015.7167013>

[27] Gold, G., Helmreich, K.: A physical surface roughness model and its applications. *IEEE Transactions on Microwave Theory and Techniques* **65**(10), 3720–3732 (2017) <https://doi.org/10.1109/TMTT.2017.2695192>